Phys. Med. Biol., 1992, Vol. 37, No 3, 587-603. Printed in the UK

Simultaneous compensation for attenuation, scatter and detector response for SPECT reconstruction in three dimensions

Z Liang, T G Turkington, D R Gilland, R J Jaszczak and R E Coleman
Department of Radiology, Duke University Medical Center, Durham, NC 27710, USA

Received 1 November 1991

Abstract. A three-dimensional reconstruction method for simultaneous compensation of attenuation, scatter and distance-dependent detector response for single photon emission computed tomography is described and tested by experimental studies. The method determines the attenuation factors recursively along each projection ray starting at the intersected source voxel closest to the detector. The method substracts the scatter energy window data from the primary energy window data for scatter compensation. The detector response is modelled to be spatially invariant at a constant distance from the detector. The method convolves source distribution with the modelled response function to compensate for the detector response. The Poisson noise is modelled by Poisson likelihood and smoothed by use of a non-uniform entropy prior to searching for the maximum *a posteriori* probability solution. The method was tested using projections acquired from a chest phantom by a three-headed detector system with parallel hole collimators. An improvement was shown in image noise, recognition of object sizes and shapes, and quantification of concentration ratios.

1. Introduction

One of the most important tasks in image reconstruction is quantitative accuracy in terms of object intensities, sizes and shapes. Quantitative accuracy in single photon emission computed tomography (SPECT) is impaired by a number of factors including noise, attenuation, scatter and detector response. The noise is a result of the limited number of detected photons. The attenuation (including absorption and deflection of primary photons due to Compton scatter) within the body lowers the number of primary photons detected, while the deflected or scattered photons, if detected, add undesirable counts to the data. The detector response to a point source in air varies with distance from the detector and so causes different blurrings at different distances. Noise reduction and compensation for attenuation, scatter and detector response have been a research topic for nuclear medicine in the past two decades. These effects have previously been addressed both individually and in combination.

There have been a number of methods proposed to handle these problems individually. Only a few are listed as examples. The noise effect can be reduced either with low-pass linear filters (Lewitt 1983) or using non-linear regularizations (Censor 1983). The attenuation can be effectively compensated given the attenuation map via either filtering methods (Bellini *et al* 1979, Glick *et al* 1991, Gullberg and Budinger 1981, Tretiak and Metz 1980) or iterative methods (Chang 1978, Gullberg *et al* 1985, 1989, Tsui *et al* 1989). The problem of scatter may be mitigated by either deconvolution

0031-9155/92/030587+17$04.50

approaches (Floyd *et al* 1985, Webb *et al* 1985) or scatter subtractions (Axelsson *et al* 1984a, Jaszczak *et al* 1984). The effect of distance-dependent detector response may be compensated either by filtering projections at different angles (Lewitt *et al* 1989, Ogawa *et al* 1988) or by tracing the projection rays at each angle which are within the detector response kernel (Formiconi *et al* 1989, Green *et al* 1988). Although approaches for simultaneous compensation of attenuation and scatter (Axelsson *et al* 1984b, Beck *et al* 1982) and of attenuation and detector response (Tsui *et al* 1988, Zeng *et al* 1991) have been reported, unified methods for simultaneous compensation of all of the effects are needed.

Unified compensation methods have previously been proposed, for example, by Floyd *et al* (1986), Liang *et al* (1988), Formiconi *et al* (1990) and Penney and King (1990). The approach of Penney and King (1990) is valid only for uniform attenuating media. The other proposed unified methods have practical limitations associated with current computer memory and speed. One difficulty with the inverse approach of Floyd *et al* (1986) for fully 3D reconstruction is the dimensions of the transform matrix. For example, to reconstruct an image array $64 \times 64 \times 32$ from projections of 64×32 acquired at 64 angles, the transform matrix requires approximately 70 Gbytes. The computational burden for tracing the Klein-Nishina formula (Liang *et al* 1988) or tracing the projection rays within the scatter kernel (Formiconi *et al* 1990) for scatter compensation is very heavy. Even if a very simple model of choosing 0 or 1 for the intersections of source voxels and projections rays were used in implementing the method of Liang *et al* (1988), the heavy computational burden remains (Liang *et al* 1989a).

In this paper, the 3D unified reconstruction method of Liang *et al* (1988) is modified to use a dual-energy-window subtraction approach (Jaszczak *et al* 1984) and convolution technique (Nussbaumer 1981) for scatter compensation. This modification based on some approximations for scatter compensation is computationally efficient compared to the line tracing methods (Formiconi *et al* 1990, Liang *et al* 1988). The intersecting lengths of projection rays in voxels, which are more appropriate than 0 or 1, are used. Although some mathematical formulae have been presented in the reference of Liang *et al* (1989a), a comprehensive description is given in the following section.

2. Methods

In this section, the compensation for attenuation, scatter and detector response and the reduction for noise in SPECT reconstruction are described. The compensation is performed via the transform matrix $\{R_{ij}\}$ (it is sometimes called the system response to a point source in the body):

$$\bar{Y}_i = \sum_{j=1}^{J} R_{ij} o_j \qquad i = 1, 2, \ldots, I \tag{1}$$

where $\bar{Y}_i$ is the noise-free datum for projection ray i, o_j is the average intensity for voxel J, I is the number of projection rays and J is the number of voxels. The value of R_{ij} depends approximately on the intersecting length, l_{ij}, of voxel j with projection ray i, the attenuation factor A_{ij} for voxel j along ray i, and the weights $\{C_{ij}\}$ of the detector response kernel and τ of the dual-energy-window subtraction: $\mathbf{R} = f(\mathbf{I}, \mathbf{A}, \mathbf{C}, \tau)$. It was mentioned in the previous section that the dimensions of matrix $\{R_{ij}\}$ are very large. The inversion is limited by computer memory and speed. An alternative approach

is to compute each element R_{ij} on-the-fly. Since $\{R_{ij}\}$ is generally spatially variant due to object-dependent attenuation and scatter within the body and distance-dependent detector response, the computational burden to trace the contribution from voxel j to projection bin i, or vice versa, is very heavy. The convolution technique can reduce the computational time if it is applicable. This is one of the objectives of this paper. The noise reduction is considered via statistical modelling.

2.1. Compensation for attenuation

To determine the attenuation factors, perfect detector resolution is assumed. The 3D reconstruction method computes the attenuation factors recursively along each projection ray starting at the intersected voxel closest to the collimator, as shown by Figure 1. For each voxel, k, the attenuation factor, A_{ik}, is computed by halving the attenuating length of that voxel and then adding to the previously accumulated attenuating length along the projection ray i starting from the intersecting point, which is represented by the closed circle closest to the detector:

$$A_{ik} = \exp\left(-\sum_{j=1}^{k-1} \mu_j l_{ij} - \tfrac{1}{2}\mu_k l_{ik} \right) \tag{2}$$

where μ_j is the average attenuation coefficient of voxel j. The intersecting lengths $\{l_{ij}\}$ are determined recursively by the method described by Siddon (1985), although alternative methods can be used to compute the lengths (Huesman *et al* 1977, Gullberg *et al* 1985). Note that the ray tracing approach may not be necessary for uniform attenuation compensation.

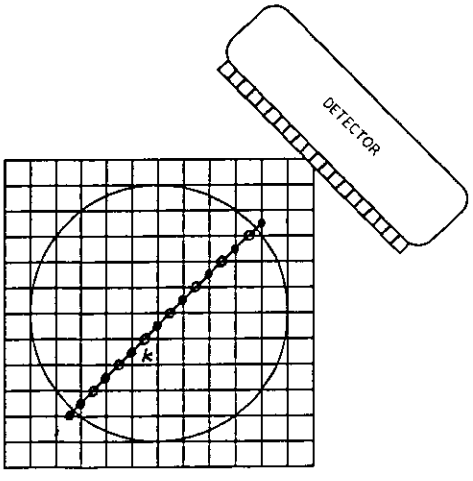

Figure 1. The 2D representation of 3D line tracing process for attenuation factors. The intersecting lengths of voxels and projection rays are the segments between open and closed circles.

2.2. Compensation for scatter

The scatter compensation approach is based on observations from experimental data. The experiment was conducted by scanning a 3.8 cm diameter sphere filled with radioactivity and placed at the centre of a chest phantom (its diagram is similar to figure 2 without the two spheres). The phantom consists of a non-uniform attenuating

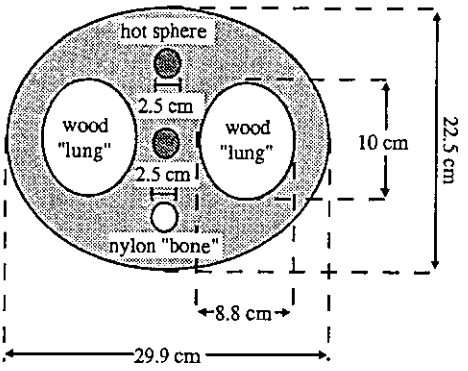

Figure 2. The cross section of a chest phantom filled with water.

media (i.e. wood, nylon and water). Dual energy windows were used in data acquisitions (Jaszczak *et al* 1984). Projections were acquired at 120 angles over 360°. Figure 3 shows the one-pixel-wide projection profiles from the primary (left) and the secondary (right) energy windows. This projection was acquired at an angle where the non-uniform attenuating media were asymmetric with respect to the sphere. The profiles were at the level of the centre of the sphere and at a normal angle to the axis of the phantom.

By observing all the projection profiles, we found that: (i) the tails of both the primary and secondary profiles were in general asymmetric and changed significantly at different projection angles; (ii) the tails of both the primary and secondary profiles were similar at each projection angle; and (iii) the central parts of the primary and secondary profiles were relatively symmetric at different angles. Observation (i) reveals that the scatter component in the primary energy window is spatially variant at a constant distance d and also at different distances, and so convolution is not applicable. Observations (ii) and (iii) suggest that the subtraction of photons of the secondary energy window from those of the primary energy window may be used for scatter compensation:

$$Y_i = Y_i^{\mathrm{p}} - \tau Y_i^{\mathrm{s}} \tag{3}$$

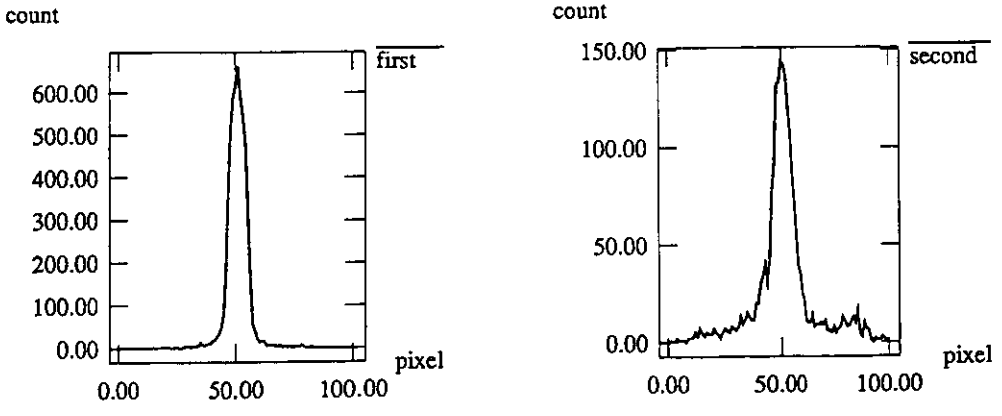

Figure 3. The projection profiles acquired using primary energy window (left) and secondary energy window (right).

where Y_i^p and Y_i^s are the data measured for projection bin i from the primary and secondary energy windows respectively. In most cases, $\tau = 0.5$ can be chosen to eliminate the asymmetrical tails of the primary profile. If the subtraction eliminates the scatter completely, the central peak of the primary profiles should be the same as those measured in air. The effect of the subtraction upon the central part of the primary profile will be discussed later.

2.3. Compensation for detector response

Since the detector response kernel, $\{C_{ij}^d\}$, for a point source in air is spatially invariant at a constant distance, d, from the detector surface, convolution of the source distribution, $\{o_j\}$, with the kernel at the same distance d can be used to compensate for the detector response:

$$\bar{Y}_i^a = \sum_j C_{ij}^d o_j \tag{4}$$

where $\bar{Y}_i^a$ is the noise-free contribution, in air, from voxels at d to projection bin i. As shown in Figure 4, the convolution is represented by the contributions of the voxels to the bin i. Each voxel contributes to those bins within the area intersected by the cone and the collimator surface. Note that, for collimators with a flat surface, those bins within each intersecting area are the same distance from the corresponding voxel. The weights or values of $\{C_{ij}^d\}$ for those bins can be characterized as a Gaussian function with width dependent on d. The weights outside the intersecting area are zero. The full-width half-maximum (FWHM) of C_{ij}^d can be obtained at the distance d by scanning a point source in air at that distance. The kernel $\{C_{ij}^d\}$ is sometimes called the system response to a point source in air. The values $\{C_{ij}^d\}$ include the geometric information of collimator holes, the intrinsic resolution of detector crystals, and the effect of collimator penetration. The geometric acceptance of collimator holes has been investigated (Tsui and Gullberg 1990).

If attenuating media are considered, the contributions from each voxel to those bins within the corresponding intersecting area are multiplied by the attenuation factors. To improve the computational efficiency, an assumption is made that, as shown in figure 5, the attenuation factor $A_{i'k}$ for voxel k and bin i' is the same as A_{ik}, where i

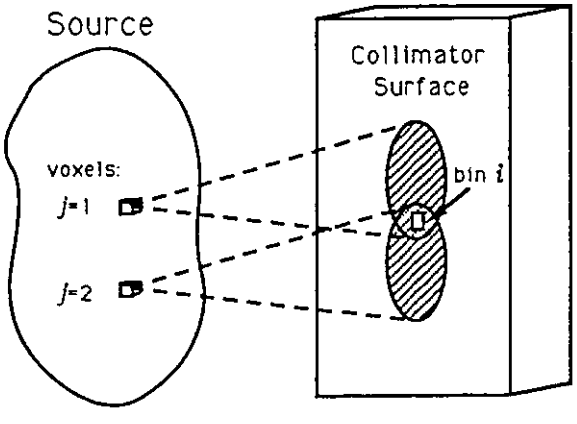

Figure 4. The geometrical representation for convolution of source and detector response kernel, in which voxels at a fixed distance contribute to projection bin i.

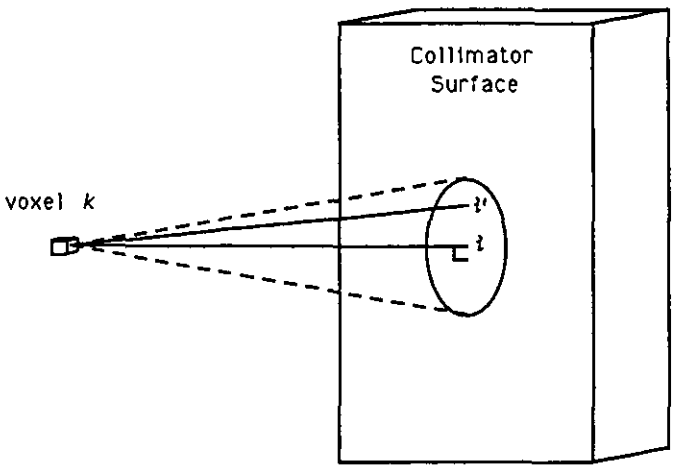

Figure 5. The geometrical representation of the convolution process, in which voxel k contributes to those projection bins within the intersecting area on the collimator surface.

represents the central bin. In other words, the attenuation factors are assumed to vary slowly within the acceptance angle of collimator holes.

The compensation for the three deterministic effects of attenuation, scatter and detector response can be summarized as follows: first the subtraction of dual-energy-window data for scatter is done before reconstruction using equation (3); then the recursive ray tracing of equation (2) and convolution of equation (4) are built into projection and back projection processes. During the projection and backprojection processes, the contribution of voxel k to a bin i' within the intersecting area or vice versa, as shown in figure 5, is computed by the product of the intersecting length l_{ik} of that voxel with ray i, the attenuation factor A_{ik} along ray i, and the weight $C^d_{i'k}$ associated with the bin i' at fixed d:

$$\text{the contribution from voxel } k \text{ to bin } i' = l_{ik}A_{ik}C^d_{i'k}.$$

The assumption made previously for detector response compensation within attenuating media is used here to improve the computational efficiency. In other words, the contribution $l_{ik}A_{ik}$ from voxel k to bin i is spread out over those bins $\{i'\}$ around the centre bin, i. The reduction for the undeterministic effect of noise is discussed below.

2.4. *Modelling of Poisson noise*

Since the photon detection noise of a Poisson nature is non-linear, a non-linear approach to minimize the noise may be appropriate. The Poisson likelihood has been widely applied in the maximum likelihood (ML) approach (Shepp and Vardi 1982):

$$P(\mathbf{Y}/\mathbf{O}) = \prod_{i=1}^{I} \exp\left(-\sum_{j=1}^{J} R_{ij}o_j\right)\left(\sum_j R_{ij}o_j\right)^{Y_i}(Y_i!)^{-1} \tag{5}$$

where R_{ij} is an element of the transform matrix mentioned before and can be defined as the proability of detecting photons in projection bin i from voxel j. The assumption made in equation (5) is that each data element, Y_i, is a Poisson variable with a mean $\Sigma_j R_{ij}o_j$ and all elements $\{Y_i\}$ are independent. The means $\{\Sigma_j R_{ij}o_j\}$ of the variables $\{Y_i\}$ reflect the relation between the acquired data and the source $\{o_j\}$ via the transform

matrix $\{R_{ij}\}$. It is noted that since the subtraction of equation (3) is used, Y_i is no longer a Poisson variable and equation (5) is an approximation for the distribution of $\{Y_i\}$.

For parallel ray geometry, the value R_{ij} can be assumed to be proportional to the intersection length of voxel j and projection ray i, if the attenuation, scatter and detector response are neglected (Budinger and Gullberg 1974, Herman 1980). This assumption is adopted. The attenuation, scatter and detector response are approximated in R_{ij} by multiplying the intersecting length, l_{ij}, with the attenuation factor, A_{ij}, and the convolution weight, C_{ij}:

$$R_{i'j} \simeq l_{ij} A_{ij} C_{i'j} \tag{6}$$

where i' and i were defined in figure 5. In practice, the proportionality factor is usually neglected for image display, because $\{o_j\}$ have to be scaled anyway. However, for quantitative evaluation of images, the factor must be considered and $R_{i'j} = f_a l_{ij} A_{ij} C_{i'j}$. The factor f_a can be expressed approximately as:

f_a = (solid angle factor of detectors) × (efficiency of detector system)

× (normalization factor of l_{ij}).

Since $\{R_{ij}\}$ are real values continuously distributed over the interval $[0, 1]$, the means $\{\Sigma_j R_{ij} o_j\}$ are continuous real values over $[0, \infty)$ regardless of $\{o_j\}$ being real or integer. Since the emissions are relatively uniform over a 4π solid angle and f_a is of the order of 10^{-4}, the values $\{R_{ij}\}$ are very small for a conventional rotating detector system and the range of average photon numbers $\{o_j\}$ emitted during the data acquisition period is relatively large on $[0, \infty)$. In this case, the truncation error between real and integer is negligible if $\{o_j\}$ are modelled as integers.

Since the matrix $\{R_{ij}\}$ is not diagonal dominant and the means $\{\Sigma_j R_{ij} o_j\}$ are spatially related to each other even if their random values $\{Y_i\}$ are assumed as spatially independent in building up the Poisson likelihood of equation (5), as well as the fact that there is noise in the measurements, additional constraints are usually needed to regularize the ill-posed property of $\{R_{ij}\}$ and to reflect the relations among $\{\Sigma_j R_{ij} o_j\}$, as well as to reduce the noise effect for a constrained and acceptable solution (Tikhonov *et al* 1977). In image restoration from blurred data and image reconstruction from projections, the spatial relations may be viewed as the correlations among nearby voxels along the projection rays due to the finite resolution of the detector system (i.e. the matrix R_{ij} is not diagonal dominant). There are many ways to impose additional constraints upon the solution (Tikhonov *et al* 1977). A natural way is to introduce an *a priori* model in searching for the maximum *a posteriori* probability (MAP) solution. Although a Gibbs-type prior can be adapted (Geman and Geman 1984), here we use a very simple multinomial prior (Liang 1988):

$$P(\mathbf{O}) = N! \left(\prod_j o_j! \right)^{-1} \prod_{j=1}^{J} [p_j]^{o_j} \qquad \text{and} \quad \sum_j p_j = 1 \tag{7}$$

where $p_j = \bar{o}_j / N$ can be chosen and $N = \Sigma_j \bar{o}_j = \Sigma_j o_j$ is a constant. The *a priori* mean $\bar{o}_j$ for voxel j may be determined by the neighbourhood of voxel j (Liang *et al* 1989b). The multinomial prior has the following properties: (i) it prohibits negative values of $\{o_j\}$; (ii) it offers the opportunity to model neighbouring correlation of voxels via $\{\bar{o}_j\}$; (iii) it is globally concave if the Stirling's approximation is used (Liang 1988); (iv) it requires $\Sigma_j o_j = N$ being conserved; and (v) it is normalized. The drawback of this

prior is the requirement that $\{o_j\}$ be integers. This requirement imposes difficulty for theoretical analysis (the Stirling's approximation is necessary) and introduces a truncation error when the source values are real and small. For SPECT application, the truncation error is small. The multinomial or non-uniform entropy prior demonstrated effectiveness in noise smoothing and edge reservation (Liang *et al* 1988).

2.5. MAP approach via the expectation–maximization algorithm

The solution to be sought is determined by maximizing the *a posteriori* probability, $P(\mathbf{O}|\mathbf{Y})$, or equivalently by maximizing the function

$$g(\mathbf{O}) = \ln P(\mathbf{O}|\mathbf{Y}) = \ln P(\mathbf{Y}|\mathbf{O}) + \ln P(\mathbf{O}) - \ln P(\mathbf{Y})$$
$$= \sum_i \left[Y_i \ln\left(\sum_j R_{ij} o_j\right) - \sum_j R_{ij} o_j \right] + \sum_j [o_j \ln(\bar{o}_j / o_j) - \ln o_j + \tfrac{1}{2} \ln(o_j - \tfrac{1}{6})]$$

where the term independent from $\{o_j\}$ was omitted and a modified Stirling's approximation for $\ln(o_j!)$ was used (Johnson 1990).

Although many numerical techniques can be employed to compute the solution which maximizes $g(\mathbf{O})$, the expectation-maximization (EM) algorithm described by Dempster *et al* (1977) is adapted (Liang *et al* 1989c):

$$o_k^{(n+1)} = o_k^{(n)} \left\{ \sum_i R_{ik} \left[Y_i \left(\sum_j R_{ij} o_j^{(n)} \right)^{-1} \right] \right\} \left(\sum_i R_{ik} (1 + Z_k^{(n)}) \right)^{-1} \tag{8}$$

where the denominator is now generalized from the original one presented previously (Liang *et al* 1989c) to $\Sigma_i R_{ik} \neq 1$ and

$$Z_k^{(n)} = -\partial \ln P(\mathbf{O}) / \partial o_k = \ln(\hat{o}_k / \bar{o}_k) + 1 + 1/\hat{o}_k - \tfrac{1}{2}(\hat{o}_k - \tfrac{1}{6})^{-1} + (\hat{o}_k / \bar{o}_k)(\hat{o}_k - \bar{o}_k)/\bar{o}_k. \tag{9}$$

The last term in equation (9) comes from the approximation of $\partial \bar{o}_k / \partial o_k \simeq (\bar{o}_k - \hat{o}_k)/\bar{o}_k$. The $\hat{o}_k$ for voxel k will be discussed later. If $\hat{o}_k < 1$, then $Z_k^{(n)} = 1$. To eliminate the free adjustable parameter we introduced previously (Liang *et al* 1989c), $\{Z_k^{(n)}\}$ are normalized to the range $(-0.5, 0.5)$ after they have been computed using equation (9).

The exact MAP-EM algorithm is given by setting $\hat{o}_k = o_k^{(n+1)}$. By such a choice, there is not a closed expression for $o_k^{(n+1)}$ as a function of $\{R_{ik}, o_k^{(n)}\}$. An approximation for $\hat{o}_k$ is needed. We tested the choice $\hat{o}_k = o_k^{(n)}$ and rejected it because it slows down convergence (Liang and Hart 1987). A general expression of $\hat{o}_k = o_k^{(n)} + \lambda(o_k^{(n)} - o_k^{(n-1)})$ was then used, which advances at nth iteration toward $(n+1)$th iteration. Such a simplified MAP-EM algorithm or Bayesian image processing (BIP) algorithm is computationally efficient. Its convergence can be proved following the recipe given by Dempster *et al* (1977). Since the adjustable parameter $\lambda \simeq 1$ cannot be determined theoretically, the choice for $\hat{o}_k$ can be further simplified as:

$$\hat{o}_k = o_k^{(n)} \left\{ \sum_i R_{ik} \left[Y_i \left(\sum_j R_{ij} o_j^{(n)} \right)^{-1} \right] \right\} \left(\sum_i R_{ik} \right)^{-1}. \tag{10}$$

This choice has two advantages; (i) the terms on the right-hand-side (RHS) of equation (10) have been computed in equation (8); and (ii) the summation of $\{\hat{o}_k\}$ can be used to normalize $\{o_k^{(n+1)}\}$ of equation (8) such that $\Sigma_k \hat{o}_k = \Sigma_k o_k^{(n+1)}$.

Since in building up the multinomial prior of equation (7) o_k was defined as the average photon number emitted from voxel k during the data acquisition period, the proportionality factor f_a should be considered in computing $Z_k^{(n)}$ when R_{ij} of equation

(6) is chosen. Since the significant terms of the RHS of equation (9) all contain the ratio $\hat{o}_k/\bar{o}_k$, the f_a dependence is cancelled. An accurate value of f_a for other less important terms is not necessary, and $f_a \simeq$ (solid angle factor of detectors) $\times$ (1/number of projection angles) may be used.

2.6. Implementation of the BIP algorithm

The implementation of the BIP algorithm of equations (8)–(10) requires the attenuation map, the detector response kernel, and the effect of dual-energy-window subtraction upon the central part of the point source response in water.

The non-uniform attenuation map for the chest phantom of figure 2 was computer generated using the sizes given in that figure. The attenuation coefficients of wood, water and nylon were assigned as 0.004/voxel, 0.036/voxel and 0.043/voxel respectively (Gilland *et al* 1991). The generated map was then slightly smoothed to reduce edge effects.

The FWHMS of the detector response kernel $\{C_{ij}^d\}$ were measured using a low-energy, ultra-high-resolution, parallel-hole collimator for a line source ($\simeq$1 mm in diameter) in air at different distances from the collimator surface. A few of them are listed in table 1.

The effect of dual-energy-window subtraction on central peak widths was measured using a point source ($\simeq$2.5 mm in diameter) in water. A detailed investigation on how many scattered photons are left in the central peak after the subtraction is beyond the scope of this work. The point source was placed at the bottom centre of a plastic cylindrical tank approximately 25 cm in diameter. The collimator was on the top of the tank and a distance of 15 cm from the source. Water was then added to the tank such that there were different water levels between the source and the collimator. The measured FWHM for the different water levels (or depths), after dual-energy-window subtraction, are shown in table 2.

The FWHM of 9.4 mm at zero depth for the point source measurement should be very close to the FWHM of 9.1 mm for the line source measurement in air at 15 cm distance after subtracting the point source size in quadrature. The result was 9.0 mm after quadrature subtraction. The other FWHM for different water depths reflect the effect of dual-energy-window subtraction upon the central peak width of the point source response in water. This effect can be easily incorporated into the detector response convolution during image reconstruction with very little computation time (see Appendix). It is noted that the effect of this subtraction on the FWHM of the point source response is not significant.

Table 1. FWHM of the detector response kernel at different distances from the collimator surface in air.

Distance (cm)	5	10	15	20	25	30
FWHM (mm)	5.3	7.0	9.1	11.3	13.0	15.3

Table 2. FWHM for different water depths at the same distance from the detector.

Depth (cm)	0	1	2	3	4	5	7
FWHM (mm)	9.4	9.2	9.3	9.4	9.5	9.6	9.8

The implementation of the BIP algorithm of equations (8)-(10) was performed, as shown by figure 6, by the following steps. (1) Storing a Gaussian response $\{T_{ik}^d\}$ as a function of FWHM and the attenuation map into computer memory. When the distance d from voxel k to projection bin i is computed in reconstruction and the water depth between voxel k and bin i is estimated (see Appendix), then the FWHM of T_{ik}^d is obtained using the measured point source response in water after the dual-energy-window subtraction and the measured line source response in air. The response kernel T_{ik}^d with this obtained FWHM as stored in computer memory is then read in for convolution. (2) Subtracting the samples of the secondary energy window from those of the primary energy window (equation (3)). (3) Setting the intial estimate of $\{o_k\}$. (4) Looping the reprojection and backprojection processes, in each of the processes, tracing the attenuation factors for each voxel k (see equation (2)) and computing the convolution contribution from each voxel k to the related projection bins or vice versa (see figure 5). The attenuation factors and convolution contribution were computed on-the-fly. Since the BIP reconstruction is stabilized, the iterative process can be terminated after a finite number of iterations, say 50 iterations.

The BIP algorithm was tested by reconstructing images from experimentally acquired projections of a chest phantom as shown by figure 2. The two 'lung' and 'bone' regions had no activity. The two same size spheres had the same amount of $^{99}Tc^m$ activity. The remaining region was filled with water containing $^{99}Tc^m$. The concentration ratio of the spheres and the 'water' background was measured to be approximately 3 to 1 by a dose calibrator. There were 120 projections acquired equally over 360°. Each projection was a 128×128 array. Only the centre 64 axial slices were used to reconstruct an image array of $128 \times 128 \times 64$. The primary energy window was centred at 140 keV with 20% width. The secondary energy window was centred at 108 keV with 35% width. The scan orbit was an ellipse. A Trionix three-headed SPECT scanner was used with

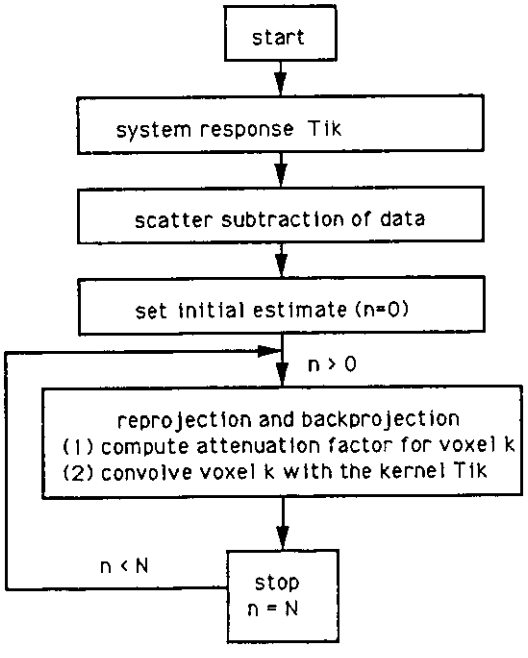

Figure 6. The flow chart for implementation of the 3D unified compensation method.

low-energy, ultra-high-resolution, parallel-hole collimators. The detector system and the dual-energy-window setting were the same as that used in the point source scanning described above. The total counts from the primary energy window were about 20 million and from the secondary energy window were about 14 million.

3. Results

The results obtained by compensating attenuation only, then with scatter subtraction using the ML-EM algorithm (Shepp and Vardi 1982) and filtered backprojection (FBP) method (Budlinger and Gullberg 1974, Herman 1980), were compared with those results obtained using the unified BIP algorithm with and without considering the *a priori* information $P(\mathbf{O})$. The computation time was about 2.5 h for one iteration on a Stellar computer GS/1000. It required about 30 Mbytes computer memories to run the reconstruction program. Most of the memories were used by the large image arrays and input data.

Figure 7 shows the cross sectional images (see figure 2), through the centres of the spheres, reconstructed using the ML-EM algorithm (i.e. set $Z_k^{(n)} = 0$ for equation (8) if the *a priori* information $P(\mathbf{O})$ is neglected) after 25 iterations. The top image was reconstructed with attenuation compensation only. This 25th iterated image was the best one as compared with those iterated from first iteration to 50 iterations by visual judgment. After 25 iterations the image became noisier. Thus a total of 25 iterations was chosen for the ML-EM algorithm in this imaging case. The middle image was obtained after 25 iterations with compensations of attenuation and scatter (i.e. the presubtraction of dual-energy-window acquisition). The bottom image considered the additional compensation of detector response (i.e. the convolution with the kernel T_{ik}^d). The curves are the profiles crossing the image centre vertically from top to bottom.

The top and middle images of figure 8 were obtained using the FBP method with a Hann filter of 0.5 cycles/pixel (or Nyquist frequency). This method offers the advantage of fast computation. The top one was compensated with attenuation only (Liang 1991). The compensation for non-uniform attenuation was performed in a similar manner to the method described by Chang (1978). The middle one was compensated with additional scatter subtraction. The curves have the same meaning as those of figure 7.

The bottom image of figure 8 was reconstructed using the BIP algorithm (i.e. equation (8) with $Z_k^{(n)} \neq 0$ for noise smoothing) after 50 iterations, which was compensated for the three effects simultaneously. Further iterated images were similar to this one. Both the bottom images of figure 7 (i.e. ML image) and figure 8 (i.e. BIP image) showed an improvement in identifying the object size and shape (i.e. the three circles of 'bone' and sphere regions). This improvement is due to the compensation of the detector response. The noise was reduced in the BIP image as compared with the ML image.

For quantitative comparison of object intensities within the reconstructed images, the intensity ratios between the objects and the background were tabulated using the cross sectional images of figures 7 and 8. The sizes for the regions-of-interests were chosen slightly smaller than the actual sizes of the 'lungs', 'bone' and 'spheres'. The intensity ratios between the 'lung' and the background, and the 'bone' with the background should be zero. The intensities of the two spheres (one was at the centre and another was near the edge) should be the same. The ratio between each sphere

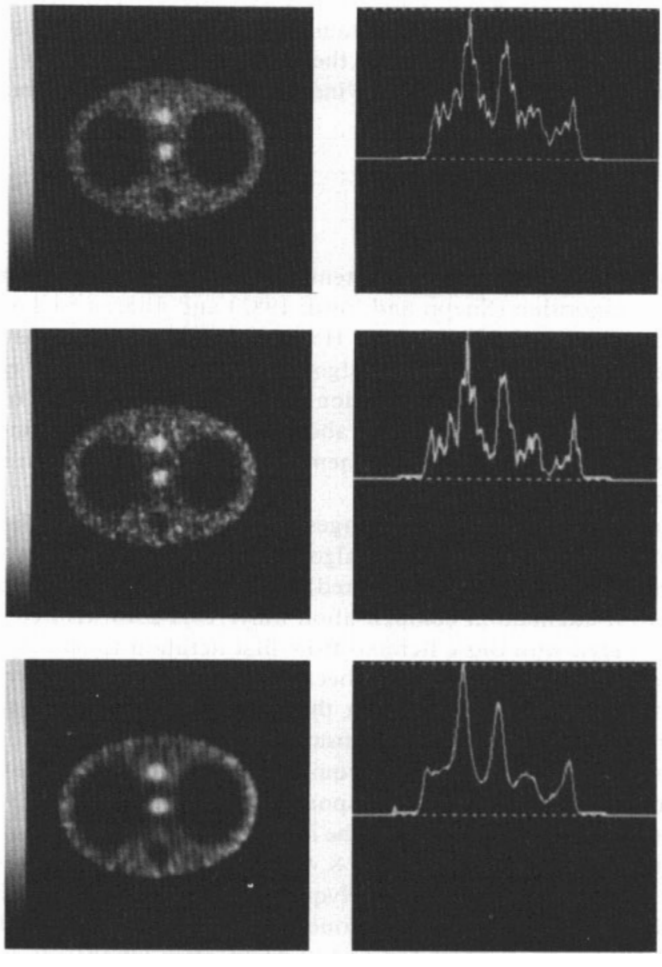

Figure 7. The slice images passing through the centre of the spheres and reconstructed using the ML-EM algorithm after 25 iterations. The curves are the profiles crossing through the image centre vertically from top to bottom. The top image was reconstructed with attenuation compensation only. The middle one was obtained with additional compensation of scatter. The bottom image further considered the compensation of detector response.

and the background should be approximately three. As shown by table 3, an improvement in quantification of intensity ratios within the BIP reconstructed image is possible.

4. Conclusions

A 3D unified reconstruction method for simultaneous compensation of attenuation, scatter and detector response for SPECT has been presented. The method was tested by experimental phantom studies. This method may improve quantification of the isotope concentration and recognition of the object sizes and shapes in reconstructed

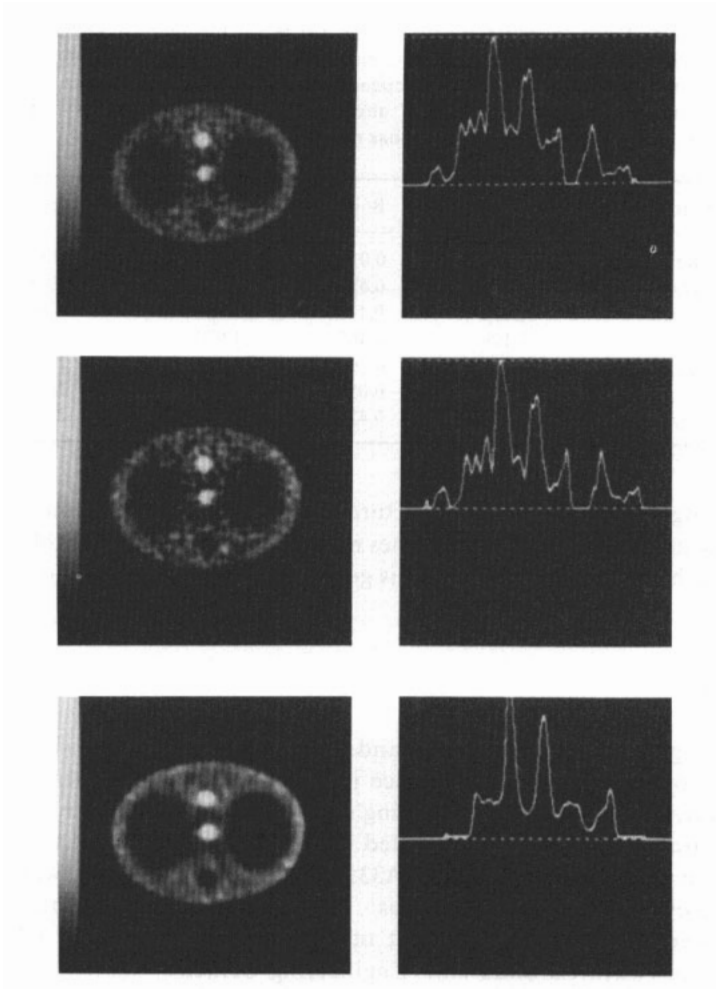

Figure 8. The slice images on the top and middle rows obtained using the FBP method with Hann filter of 0.5 Nyquist frequency. The top one compensated attenuation only. The middle one compensated additional scatter. The bottom image reconstructed using the BIP algorithm after 50 iterations. This image compensated the three effects simultaneously. The curves are the profiles crossing the image centre vertically.

images, at least for objects of increased intensity levels compared to the background. For clinical application, implementing the method requires the attenuation map. Although the measurement for the point source response in air and water is very time consuming, the measured data should be the most accurate. The convolution approach for distance-dependent detector response can be applied to positron emission tomography. Although the method was implemented for parallel beam geometry, it is theoretically straightforward to extend to cone beam geometry (Liang *et al* 1988, Zeng *et al* 1991). It may be easier to specify an *a priori* model in image space for a MAP approach to suppress noise while preserving edges (or resolution), as compared to specify a filter in frequency space for a FBP approach. However, if the *a priori* model is not appropriate, MAP can significantly decrease resolution and generate distortion in reconstruction. Since the non-uniform entropy prior does not assume any

Table 3. The intensity ratios between the objects (i.e. the 'lungs', 'bone', and spheres) and the 'water' background (bk). ML(A) means ML image with compensation of attenuation. ML(A,S) means ML image with compensation of attenuation and scatter. ML(A,S,C) means ML image with compensation of attenuation, scatter and detector response. FBP(A), FBP(A,S), and BIP(A,S,C) have similar meanings.

Ratio(isotope):	Lung/bk	Bone/bk	sphere(ctr)/bk	sphere(edge)/bk
True ratio	0.0	0.0	3.0	3.0
ML(A)	0.154	0.623	1.563	1.805
ML(A,S)	0.133	0.441	1.734	2.098
ML(A,S,C)	0.129	0.462	1.970	2.333
FBP(A)	0.335	0.200	1.735	2.054
FBP(A,S)	0.281	−0.058	2.050	2.546
BIP(A,S,C)	0.092	0.439	2.508	2.577

specific knowledge about the image structure (e.g. piecewise contiguous image) and the implementation of the BIP algorithm does not require any free adjustable parameter, the MAP approach described in this paper is generally applicable in practical solutions.

Acknowledgments

The authors are grateful to Mr K Greer and Dr H Wang for their assistance in data acquisition. Dr M Smith for his assistance in preparing this manuscript, and Dr V Johnson for providing the modified Stirling's approximation. This investigation was supported by Grant No. HL44194, awarded by the National Heart, Lung and Blood Institute, and in part by Grant Nos. CA33541 and S10-RR04176, awarded by the National Cancer Institute, Grant Nos DE-FG05-90ER75577 and DE-FG05-91ER60894, awarded by the Department of Energy, and Grant No. CDR-862201, awarded by Duke North Carolina NSF Engineering Center.

Appendix

Since the measurements for a point source at different distances from the detector and at variance depths in water are very time consuming, the FWHM of T_{ik}^{d} is estimated as follows using the measured FWHM of tables 1 and 2.

From the measured FWHMs at different depths in water for the point source at the distance of 15 cm from the collimator surface (see table 2), a linear fitting using the least-square method results in

$$\text{FWHM}(d') = 9.2 + 0.075\, d' \tag{A1}$$

where d' is the depth in water. At zero depth, there is no scatter, FWHM = 9.2 mm, i.e. the detector blurring in air at the distance of 15 cm for the point source. At other depths, the scatter broadened the FWHM, and the results are computed, by subtracting 9.2 in quadrature (see table A1).

This effect due to scatter subtraction is easily compensated in the detector response convolution during image reconstruction. First the attenuation length $\Sigma_j \mu_j l_{ij} + \frac{1}{2}\mu_k l_{ik}$ is

Table A1. The broadening in FWHM at different water depths.

Depth (cm)	0	1	2	3	4	5	7
FWHM (mm)	0.0	1.2	1.7	2.1	2.4	2.7	3.2

computed for voxel k along projection ray i for attenuation correction (see equation (2)). The depth d' in water for the voxel k and bin i is then estimated by dividing the attenuation length by the attenuation coefficient of water. For example, photons emitted from voxel k pass 5 cm air (or lung with attenuation coefficient $\mu_a = 0$) and 3 cm water (or soft tissues with attenuation coefficient μ_w) to reach bin i, then the attenuation length $= 5\mu_a + 3\mu_w = 3\mu_w$ and the depth in water $d' = 3$ cm. Once the depth d' is known, the FWHM of T_{ik}^d can be determined from the FWHM of C_{ik}^d in table 1 and the FWHM in table A1: $\text{FWHM}^2_{T_{ik}} = \text{FWHM}^2_{C_{ik}} + \text{FWHM}^2_{\text{table A1}}$. Finally the convolution contribution of voxel k to those bins around bin i in the distance d is computed (see figure 5).

Résumé

Compensation simultanée pour l'atténuation, la diffusion et la réponse du détecteur en reconstruction SPECT en trois dimensions.

Les auteurs décrivent une méthode de reconstruction tridimensionnelle prenant en compte simultanément la compensation de l'atténuation, de la diffusion et de la réponse du détecteur, dépendant de la distance, pour la tomographie d'émission en simple photon. Ils ont testé cette méthode à l'aide d'études expérimentales. La méthode détermine de façon récursive le facteur d'atténuation le long de chaque rayon de projection à son intersection avec le voxel source le plus près du détecteur. La méthode soustrait les données de la fenêtre en énergie du diffusé des données de la fenêtre en énergie du rayonnement primaire pour la compensation du diffusé. La modélisation de la réponse du détecteur suppose qu'elle est spatialement invariante pour une distance constante du détecteur. La méthode convolue la distribution de la source avec la fonction de réponse modélisée pour compenser de la réponse du détecteur. Le bruit poissonien est modélisé par la probabilité poissonienne, et lissé par l'utilisation d'une entropie non uniforme préalable à la recherche du maximum de probabilité *a postériori*. La méthode a été testée en utilisant les projections acquises pour un fantôme de thorax par un système à trois têtes, avec des collimateurs à canaux parallèles. Une amélioration a été montrée en ce qui concerne le bruit de l'image, la reconnaissance des tailles et des formes des objets et la quantification des rapports de concentration.

Zusammenfassung

Simultaner Ausgleich von Schwächung, Streuung und Detektoransprechvermögen von SPECT Rekonstruktionen in drei Dimensionen.

Eine dreidimensionale Rekonstruktionsmethode zum simultanen Ausgleich von Schwächnung, Streuung und Detektoransprechvermögen in der Einzel-Photon-Emissionscomputertomographie wird beschrieben und überprüft durch experimentelle Untersuchungen. Die Methode bestimmt die Schwächungsfaktoren rekursiv entlang eines jeden Projecktionsstrahls, angefangen beim dem Quellenvoxel, der dem Detektor am nächsten liegt. Bei der Methode werden die Werte des Streuenergiefensters von den Werten des Primärenergiefensters zur Kompensierung der Streuung subtrahiert. Das Detektorverhalten wird räumlich invariant in konstantem Abstand vom Detektor simuliert. Bei der Methode wird die Quellenverteilung gefaltet mit der Responsefunktion, um so das Detektoransprechvermögen auszugleichen. Das Poissonrauschen wird modeliert nach der Poisson-Likelihood-Methode und geglättet durch Verwendung einer inhomogenen Entropie, bevor die maximale *a posteriori* Wahrscheinlichkeitslösung gesucht wird. Die Methode wurde

getestet mit Projektionen, die man durch ein Oberkörperphantom mit Hilfe von einem dreiköpfigen Detektorsystem mit Parallellochkollimatoren erhielt. Es zeigte sich eine Verbesserung bezüglich des Bildrauschens, der Erkennbarkeit von Objecktgröße und -form und der Quantifizierung der Konzentationsverhältnisse.

References

Axelsson B, Israelsson A, Larsson S and Msaki P 1984b Attenuation and scatter correction aiming at quantitative SPECT *Proc. Int. Annual Mtg of SNM (Europe)* vol 22 pp 23–6

Axelsson B, Msaki P and Israelsson A 1984a Subtraction of Compton scattered photons in SPECT *J. Nucl. Med.* **25** 490–4

Beck J, Jaszczak R, Coleman E, Starmer C and Nolte L 1982 Analysis of SPECT including scatter and attenuation using sophisticated Monte Carlo modeling methods *IEEE Trans. Nucl. Sci.* **NS-29** 506–11

Bellini A, Piacentini M, Cafforio C and Rocca F 1979 Compensation of tissue absorption in emission tomography *IEEE Trans. Acoustics, Speech and Signal Processing* **ASSP-27** 213–8

Budinger T and Gullberg G 1974 Three-dimensional reconstruction in nuclear medicine emission imaging *IEEE Trans. Nucl. Sci* **NS-21** 2–20

Censor Y 1983 Finite series-expansion reconstruction methods *Proc. IEEE* **71** 409–19

Chang L 1978 A method for attenuation correction in radionuclide computed tomography *IEEE Trans. Nucl. Sci.* **NS-25** 638–43

Dempster A, Laird N and Rubin D 1977 Maximum likelihood from incomplete data via the EM algorithm *J. R. Stat. Soc.* **38** 1–38

Floyd C, Jaszczak R. Greer K and Coleman E 1985 Deconvolution of Compton scatter in SPECT *J. Nucl. Med.* **26** 403–8

—— 1986 Inverse Monte Carlo as a unified reconstruction algorithm for ECT *J. Nucl. Med.* **27** 1577–85

Formiconi A, Passeri A, Pupi A and Comis G 1990 High resolution brain SPECT with accurate modeling of spatial system response, attenuation and scatter *J. Nucl. Med.* **31** 739

Formiconi, A, Pupi A and Passeri A 1989 Compensation of spatial system response in SPECT with conjugate gradient reconstruction technique *Phys. Med. Biol* **34** 69–84

Geman S and Geman D 1984 Stochastic relaxation, Gibbs distributions, and the Bayesian restoration of images *IEEE Trans. Pattern Analysis and Machine Intelligence* **PAMI-6** 721–41

Gilland D, Jaszczak R, Greer K and Coleman E 1991 Quantitative SPECT reconstruction of iodine-123 data *J. Nucl. Med.* **32** 527–33

Glick S, Penney B and King M 1991 Filtering of SPECT reconstructions made using Bellini's attenuation correction method: a comparison of three pre-reconstruction filters and a post-reconstruction Wiener filter *IEEE Trans. Nucl. Sci* **NS-38** 663–69

Green A, Begent R and Bagshawe K 1988 Maximum likelihood reconstruction incorporating line spread function data *Eur. J. Nucl. Med.* **14** 226

Gullberg G and Budinger T 1981 The use of filtering methods to compensate for constant attenuation in SPECT *IEEE Trans. Biomed. Eng.* **BME-28** 142–57

Gullberg G. Huesman R, Malko J, Pelc N and Budinger T 1985 An attenuated projector-Backprojector for iterative SPECT reconstruction *Phys. Med. Biol.* **30** 799–816

Gullberg G, Zeng G, Tsui B and Hagius J 1989 An iterative reconstruction algorithm for SPECT with cone beam geometry *Int. J. Imaging Sys. Tech.* **1** 169–86

Herman G 1980 *Image Reconstruction from Projections: the Fundamentals of Computerized Tomography* (New York: Academic)

Huesman R, Gullberg G, Greenberg W and Budinger T 1977 *User manual: donner algorithm for reconstruction tomography (Lawrence Berkeley Laboratory Publication)*

Jaszczak R, Greer K, Floyd C, Harris C and Coleman R 1984 Improved SPECT quantification using compensation for scattered photons *J. Nucl. Med.* **25** 893–900

Johnson V 1990 Private communication

Lewitt R 1983 Reconstruction algorithms: transform methods *Proc. IEEE* **71** 390–408

Lewitt R, Edholm P and Xia W 1989 Fourier method for correction of depth-dependent collimator blurring *SPIE Med. Imaging III* **1092** 232–43

Liang Z 1988 Statistical models of *a priori* information for image processing *SPIE Med. Imaging II* **914** 677–83

—— 1991 Implementation of linear filters for iterative penalized maximum likelihood SPECT reconstruction *IEEE Trans. Nucl. Sci.* **NS-38** 600–11

Liang Z and Hart H 1987 Bayesian image processing of data from constrained source distributions: I Non-valued, uncorrelated and correlated constraints *Bull. Math. Biol.* **49** 51–74

Liang Z, Jaszczak R, Floyd C, Greer K and Coleman R 1988 Bayesian reconstruction of SPECT in parallel, fan and cone beam geometries *J. Nucl. Med.* **29** 871

Liang Z, Jaszczak R, Floyd C, Greer K and Coleman R 1989a Reprojection and backprojection in SPECT image reconstruction *Proc. IEEE Energy Inform. Tech. Southeast* **1** 919–26

Liang Z, Jaszczak R, Floyd C 1989b A spatial interaction model for statistical image processing *Proc. Inform Process. Med. Imaging* **11** 29–43

Liang Z, Jaszczak R and Greer K 1989c On Bayesian image reconstruction from projections: uniform and non-uniform *a priori* source information *IEEE Trans. Med. Imaging* **MI-8** 227–35

Nussbaumer H 1981 *Fast Fourier Transform and Convolution Algorithms* (New York: Springer)

Ogawa K, Paek S, Nakajima M, Yuta S, Kubo A and Hashimoto S 1988 Correction of collimator aperture using a shift-variant deconvolution filter in gamma camera emission CT *SPIE Med. Imaging II* **914** 699–706

Penney B and King M 1990 A projector, back-projector pair which accounts for the 3D depth and distance dependent blurring in SPECT *IEEE Trans. Nucl. Sci.* **NS-37** 681–6

Shepp L and Vardi Y 1982 Maximum likelihood reconstruction for emission tomography *IEEE Trans. Med. Imaging* **MI-1** 113–22

Siddon R 1985 Fast calculation of the exact radiological path for a 3D CT array *Med. Phys.* **12** 252–5

Tikhonov A, Arsenin V and John F 1977 *Solutions of Ill-Posed Problems* (New York: Wiley)

Tretiak O and Metz C 1980 The Exponential Random Transform *SIAM J. Appl. Math.* **39** 341–53

Tsui B and Gullberg G 1990 The geometric transfer function for cone and fan beam collimators *Phys. Med. Biol* **35** 81–93

Tsui B, Gullberg G, Edgerton E, Ballard J, Perry J, McCartney W and Berg J 1989 Correction of nonuniform attenuation in cardiac SPECT imaging *J. Nucl. Med.* **30** 497–507

Tsui B, Hu H, Gilland D and Gullberg G 1988 Implementation of simultaneous attenuation and detector response correction in SPECT *IEEE Trans. Nucl. Sci.* **NS-35** 778–83

Webb S, Long A, Ott R, Leach M and Flower M 1985 Constrained deconvolution of SPECT liver tomograms by direct digital image restoration *Med. Phys.* **12** 53–8

Zeng G, Gullberg G, Tsui B and Tarry J 1991 Three-dimensional iterative reconstruction algorithms with attenuation and geometric point response correction *IEEE Trans. Nucl. Sci.* **NS-38** 693–702